

# Mixed-dimensional modeling of delamination in rare earth-barium-copper-oxide coated conductors composed of laminated high-aspect-ratio thin films

Peifeng Gao<sup>1,2</sup>, Wan-Kan Chan<sup>1</sup> , Xingzhe Wang<sup>2</sup> and Justin Schwartz<sup>1,3</sup> 

<sup>1</sup> Department of Materials Science & Engineering, North Carolina State University, Raleigh, NC 27695, United States of America

<sup>2</sup> Key Laboratory of Mechanics on Western Disaster and Environment, Ministry of Education, College of Civil Engineering and Mechanics, Lanzhou University, Lanzhou 730000, People's Republic of China

<sup>3</sup> College of Engineering, Pennsylvania State University, University Park, PA 16802, United States of America

E-mail: [wchan@ncsu.edu](mailto:wchan@ncsu.edu)

Received 3 March 2018, revised 1 May 2018

Accepted for publication 16 May 2018

Published 13 June 2018



## Abstract

Rare earth-barium-copper-oxide (REBCO) coated conductors are promising conductors for high energy, high field and high temperature superconducting applications. In the case of epoxy-impregnated REBCO superconducting coils, however, excessive transverse stresses generated from winding, cooling, and Lorentz forces on the REBCO conductors can cause delamination, resulting in reduction in the load-carrying capacity as well as significant degradation in the coil's critical current. In this study, the stresses and strains, and delamination in a REBCO conductor are analyzed via a mixed-dimensional finite element method (FEM) based on the cohesive zone model (CZM). The mixed-dimensional method models any number of laminated high-aspect-ratio thin layers in a composite as stacked two-dimensional (2D) surfaces, thus, resolving the thickness-dependent meshing and computational problems in modeling such composites with full three-dimensional (3D) FEM approaches. In the studied coated conductor, the major thin constituent layers, namely, the silver, REBCO and buffer layers, are modeled as 2D surfaces while the relatively thick stabilizer and substrate are in 3D layers. All the adjacent layers are coupled via spring equations under the CZM framework. The mixed-dimensional delamination model is validated by a full-3D FEM counterpart model. Simulation results show that the mixed-dimensional model performs simulations with much higher computational efficiency than the full-3D counterpart while maintaining sufficient accuracy. Effects of the anvil size and initial crack size on delamination behavior are discussed and compared to experimental phenomena. Furthermore, the stress distributions of the constituent layers of the conductor under different delamination initiation sites are predicted.

**Keywords:** cohesive zone model, REBCO coated conductor, delamination modeling, mixed-dimensional modeling method

(Some figures may appear in colour only in the online journal)

**List of nomenclature**

Parameter	Description		
$u_i$	Relative separation displacement in $i$ (normal or shear) direction	$E_3$	Through-thickness effective elastic property of the composite
$\sigma_i$	Interfacial traction stress in $i$ direction	$t$	Thickness of an adjacent sub-laminate layer
$K$	Initial penalty stiffness	$E$	Young's modulus
$u_i^0$	Damage initiation separation in $i$ direction	$\nu$	Poisson's ratio
$\sigma_i^0$	Interfacial cohesive strength (interfacial traction stress corresponding to the damage initiation) in $i$ direction	$\sigma_y$	Yield strength
$u_i^f$	Ultimate failure separation in $i$ direction	$E_t$	Tangent modulus
$G_{ic}$	Critical fracture energy release rate in $i$ direction	$w_{\text{tape}}$	Tape width
$u_i^{\max}$	Current maximum separation displacement in $i$ direction	$l_{\text{tape}}$	Tape length
$u_{i,\text{old}}^{\max}$	Maximum separation displacements in $i$ direction recorded from the previous time step	$w_{\text{anvil}}$	Anvil width
$K'$	Updated penalty stiffness	$l_{\text{anvil}}$	Anvil length
$D_i$	Damage evolution function of penalty stiffness in $i$ direction	$S_d$	Anvil section area
$G_i$	Energy release rate in $i$ direction	$E_{\text{sys}}$	Energy of the entire system
$\alpha$	Power exponent of ultimate failure power law criterion	$F_e$	External transverse force load
$u_{i,k}$	Relative separation displacement of interface $k$ in $i$ direction	$d_l$	Applied load displacement
$u_i^k$	Displacement of surface $k$ in $i$ direction	$E_{\text{del}}$	Release energy induced by delamination
$u_m$	Mixed-mode relative separation displacement	$E_{\text{str}}$	Release energy induced by strain energy
$\beta$	Mode mixity ratio	$l_p$	Position in longitudinal direction
$u_m^{n0} (u_m^{s0})$	Normal (shear) relative separation displacements corresponding to damage initiation under mixed-mode loading	$F_p$	Peel force per unit width
$u_m^{nf} (u_m^{sf})$	Normal (shear) relative separation displacements corresponding to ultimate failure under mixed-mode loading	$\gamma$	Debonding energy
$u_m^0$	Damage initiation separation under mixed-mode loading	$\varphi$	Work expenditure rate per unit advance of the peel propagation
$u_m^f$	Ultimate failure separation under mixed-mode loading	$\sigma_t$	Applied transverse tensile stress
$u_m^{\max}$	Current maximum mixed-mode separation displacement	$l_{\text{pre}}$	Pre-crack length
$u_{m,\text{old}}^{\max}$	Maximum mixed-mode separation displacement recorded from previous time step	<b>Subscript</b>	
$\sigma_m^p$	Stress component of interfacial traction stress in the $p$ principal direction of the stress tensor under mixed-mode loading	$i = n, s$	$n$ for normal and $s$ shear (and tearing) directions
$u_m^q$	Relative displacement in the $q$ principal direction under mixed-mode loading	$k$	Interface number ( $k = 1, 2, 3, 4$ )
$K'_m$	Updated penalty stiffness under mixed-mode loading	<b>Superscript</b>	
$D_m$	Damage evolution function of penalty stiffness under mixed-mode loading	$0, f$	$0$ for damage initiation and $f$ ultimate failure
		$k, k + 1$	Surface numbers of in-contact surfaces ( $k = 1, 2, 3, 4$ )
		$p, q$	One of the three principal directions ( $p, q = 1, 2, 3$ )

**1. Introduction**

The high temperature superconducting (HTS) rare earth-barium-copper-oxide (REBCO) coated conductors are promising conductors for high energy, high field and HTS applications such as magnetic energy storage and nuclear magnetic resonance and fusion reactors [1–6].

Although REBCO conductors possess excellent uniaxial tension strength due to their strong substrates, fabrication, cooling [7, 8], Lorentz forces [9, 10], quench, and fatigue could induce large stresses and strains to the constituent layers. Experimental results showed that the typical stress

limit in the longitudinal direction is about 700 MPa for IBAD/MOCVD conductors at liquid nitrogen temperature [11, 12], which is higher than the hoop stress generated by Lorentz forces in a 30.53 T background field [13]. As in typical laminated composite materials, however, delamination is a common failure mode that seriously affects conduction performance of REBCO conductors. Once one of the brittle constituent layers, i.e., the REBCO and buffer layers, fails under large stresses or strains, significant degradations in the superconducting and electromechanical properties occur irreversibly.

Many investigations have been attempted to explore the delamination behavior of REBCO conductor tapes. Methods for measuring delamination strength include the anvil and pin-pull transverse tension tests [14–19], peel test [20, 21], cleavage test [22], and anvil shear test [23]. The initial anvil transverse tension work in [14] reported the delamination strength, defined as the maximum transverse tensile stress at which the ceramic layers delaminate from one another, is around 15 MPa. The experimental results in [23] showed that delamination strength could be reinforced by laminating strips and adding solder fillets at the conduction edges, however, the conductor tape slitting procedure in the production process played an important role in causing delamination failure. Delamination due to radial stresses occurred during a cooling process in epoxy-impregnated double pancake coils, as observed in [15]. By using scanning electron microscope and energy dispersive spectroscopy, it was found that the conductor was either debonded with a ‘mixed-mode’ delamination mode on the interface between the buffer and REBCO layers, or fractured in the REBCO layer itself. Similar results on delamination sites were reported in [16] through pin-pull transverse tension tests.

A systematic study on the REBCO conductor delamination via experiments and numerical analysis was reported in [17, 18]. The delamination strength increased with smaller anvil size for both RCE-DR and MOCVD conductors [17]. The corresponding two-dimensional (2D) numerical analysis showed that the REBCO layer experienced the largest stress with an anvil covering the entire conductor width, which could result in low delamination strength [18]. With small anvils, the copper stabilizer layer was subjected to the largest stress among all the constituent layers, which could result in higher delamination strength [18]. Moreover, the numerical results in [19] reported delamination at the interface between the REBCO/buffer layer and Hastelloy by a full three-dimensional (3D) finite element model (FEM) model.

Peel tests at various peel angles were first carried out in [20], and the test results indicated that the peel strength and the weakest interface were strongly related to the peel angles and silver annealing method. As for delamination induced by cleavage stress, a thorough study using experiments and FEM analysis was reported in [22]. Results showed that delamination induced by cleavage stress occurred at the buffer–Hastelloy interface, and cracks and micro-peels existing on the slit edge led to significant reduction in cleavage strength.

Most recently, [23] reported results on delamination behavior induced by shear stress at room temperature (RT) and 77 K. The test data showed that the average shear strength for samples with no slit edge was higher than with a slit edge, and the average shear strengths at 77 K were higher than those at RT [23]. FEM simulations showed that the stress concentration near the anvil edge resulted in delamination and the shear strength in the REBCO layer was about 30–60 MPa for different anvil sizes [23].

Most REBCO conductor delamination studies focused on experiments under transverse tension stress or shear stress [14–17, 19–23]. Through experiments, only some conductor level results are obtained, such as delamination strength and failure location. Yet it remains difficult to observe any stress distribution details on each constituent layer within the conductor. Thus, a computational approach is necessary to study micro-level stress distributions on each constituent layer during delamination and crack propagation. As typical REBCO conductors contain laminated high-aspect-ratio (HAR) thin films, such as the silver, REBCO, and buffer layers, effective modeling is a significant challenge. This is mainly because the number of non-degenerated finite elements required to approximate geometrically, with sufficient accuracy, a composite that contains HAR thin layers would be enormously large. Direct meshing of the thin layers and scaling to reduce the aspect ratio [18, 19, 23, 24] are some common practices in treating thin layers computationally. Prior FEM analyses of stress distributions on constituent layers of a REBCO conductor under transverse tension or shear load [18, 19, 23] either did not include all the major constituent thin film layers or were not based on delamination modeling techniques. For example, it is common that the REBCO and buffer layers are considered as a single layer to reduce the difficulty of modeling separately the laminated thin films [18, 19, 23]. Experimental results, however, showed that one of the typical delamination sites is the interface between the REBCO and buffer layers. Merging the two components into one layer loses the most important information at the REBCO–buffer interface, leading to inaccurate results.

In the present study, an FEM model of REBCO conductor delamination, based on the cohesive zone model (CZM) coupled with elastoplastic material properties, is developed to study the generation and propagation behavior of delamination in REBCO coated conductors. A 3D/2D mixed-dimensional modeling approach, which has been successfully applied to quench simulations of coated conductor tapes [25, 26], is used as an efficient and viable way to overcome the meshing and computational problems associated with modeling HAR laminated thin film layers in FEM. The key technique of the mixed-dimensional approach is to model the laminated HAR thin film layers, namely, the silver, REBCO and buffer layers, as 2D laminated surfaces, independent of the thickness of each layer. The mixed-dimensional approach also allows complicated coils models to be built by repeatedly applying the same 3D/2D





[30, 31, 34] as:

$$\left( \frac{\langle \sigma_n \rangle}{\sigma_n^0} \right)^2 + \left( \frac{\sigma_s}{\sigma_s^0} \right)^2 = 1, \quad (9)$$

where the symbol  $\langle \rangle$  is the Macaulay operator defined as:

$$\langle x \rangle = \begin{cases} 0, & x < 0 \\ x, & x \geq 0 \end{cases}. \quad (10)$$

When equation (9) is satisfied, the interfacial damage initiation (debonding) caused by normal and/or shear modes occurs. The function  $\langle \sigma_n \rangle$  in equation (10) ensures that a compressive normal stress does not induce a damage onset.

Once the initiation criterion (equation (9)) is reached, delamination propagation under mixed-mode loading is predicted by the satisfaction of a commonly used ‘power law’ criterion [30, 31]:

$$\left( \frac{G_n}{G_{nc}} \right)^\alpha + \left( \frac{G_s}{G_{sc}} \right)^\alpha = 1, \quad (11)$$

where  $G_n$  and  $G_s$  are the energy release rates in the normal and shear directions under mixed-mode loading, respectively. Here the power exponent  $\alpha$  is chosen to be 1.

## 2.2. Finite element delamination models

The 3D/2D mixed-dimensional delamination model for REBCO conductor tapes is implemented in FEM with COMSOL Multiphysics. The model is based on Superpower’s REBCO conductor and includes all the main constitute layers, including the stabilizer, substrate, and the laminated thin films, namely, the silver, REBCO, and buffer layers, as shown in figure 2. Similar to [25–27], the HAR thin film layers are modeled as 2D surfaces while the relatively thick stabilizer and substrate are implemented in 3D domains. This mixed-dimensional modeling approach overcomes the difficulties in modeling 3D HAR thin layers in mesh-based numerical methods such as FEM. An isotropic, bilinear Hooke’s law spring connection formulated under the CZM framework is used to bind two in-contact adjacent surfaces on an interface in which delamination may occur. The constitutive relationship of the bilinear spring connection is described by equations similar to equations (5)–(8); more details follow.

Referring to figure 2, the relative separation displacement  $u_{i,k}$  on interface  $k$  located between two in-contact surfaces  $k$  and  $k + 1$ , for  $k = 1, \dots, 4$ , is

$$u_{i,k} = u_i^k - u_i^{k+1}, \quad i = n, s. \quad (12)$$

In COMSOL, an ‘identity pair’ is used to correlate two in-contact but otherwise independent surfaces by specifying the two surfaces as ‘pair’ with one as the ‘source’ surface and the other as the ‘destination’ surface, and using pairing functions  $src2dst\_pn(u)$  and  $dst2src\_pn(u)$  to extract the values of the variable  $u$  on the source and destination surfaces, respectively. Here ‘\_pn’ is a unique but otherwise arbitrary pair identity name. The pairing functions allow

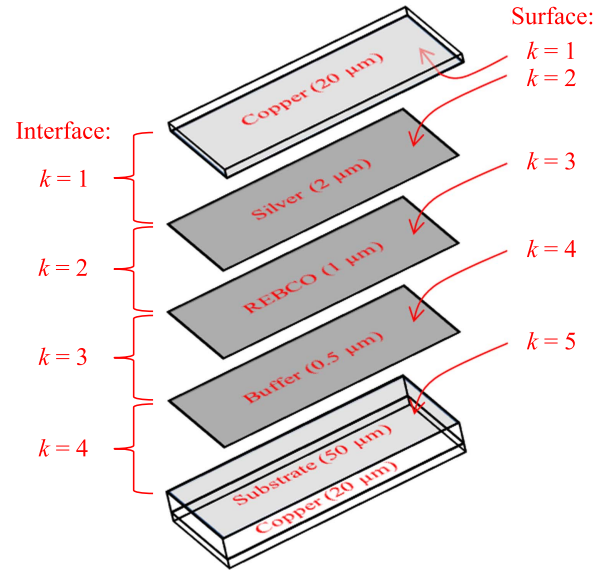


**Figure 2.** A representative implementation of a 3D/2D REBCO conductor tape model. Thicknesses of the physical layers and names of the surfaces and interfaces are shown.

special boundary equations to be defined between any two paired in-contact surfaces and implemented in weak form. In figure 2, the two adjacent surfaces  $k$  and  $k + 1$  on the interface  $k$ , for  $k = 1, \dots, 4$ , are paired with an identity pair unique to that interface. In general, any number of laminated surfaces can be modeled in this way. The CZM-based bilinear spring connection between surface  $k$  and  $k + 1$  is implemented as a ‘spring foundation’ (COMSOL terminology) boundary equation in a 3D/2D model. The ‘ground’ in the spring foundation is manually changed to the displacement of the  $k$  surface, while the other end of the spring is connected to the  $k + 1$  surface. In a full-3D counterpart model, which is used to validate the 3D/2D model, no pair is needed on each interface and the CZM-based bilinear spring connection is implemented as an internal ‘thin elastic layer’ (COMSOL terminology) boundary condition. The equations for the modified spring foundation and the thin elastic layer are equivalent. The paired boundary equation serves as the mechanism to couple two laminated, independent layers, either as a 2D surface or a 3D layer, together in the mixed-dimensional model.

Since all the delaminating interfaces can be described by the same set of CZM constitutive equations, except with differences only in the subscript  $k$ , hereafter, for simplicity, the subscript  $k$  is dropped in all the equations, e.g.,  $u_{i,k}$  is simply written as  $u_i$ . Delamination in a REBCO conductor tape induced by peeling and transverse anvil pull involves mixed-mode loading and thus mixed-mode CZM is implemented in the delamination models. The mixed-mode relative separation displacement  $u_m$  is defined as:

$$u_m = \sqrt{u_n^2 + u_s^2}. \quad (13)$$

As adjacent layers connected by springs, the traction stresses before damage onset are:

$$\sigma_n = Ku_n, \quad (14)$$

$$\sigma_s = Ku_s. \quad (15)$$

According to equation (1), the single-mode damage onset displacements can be calculated as:

$$u_n^0 = \frac{\sigma_n^0}{K}, \quad (16)$$

$$u_s^0 = \frac{\sigma_s^0}{K}. \quad (17)$$

Define the mode mixity ratio as:

$$\beta = \frac{u_s}{u_n} \quad (18)$$

then by substituting equations (13)–(18) into (9), the mixed-mode damage initiation criterion is governed by:

$$u_m^0 = \begin{cases} u_n^0 u_s^0 \sqrt{\frac{1 + \beta^2}{(u_n^0)^2 + (\beta u_n^0)^2}} & u_n \geq 0 \\ u_s^0 & u_n < 0 \end{cases}. \quad (19)$$

Note that single-mode damage initiation separations are included in equation (19). In particular, the normal mode criterion is obtained by setting  $\beta = 0$  to get  $u_m^0 = u_n^0$ , and the shear model criterion by setting  $\beta = \infty$  to get  $u_m^0 = u_s^0$ .

The energy release rates corresponding to delamination (complete debonding) in the normal and shear directions under mixed-mode loading, i.e.,  $G_n$  and  $G_s$ , in equation (11) are obtained from:

$$G_n = \int_0^{u_m^{nf}} \sigma_n du_n = \frac{Ku_m^{nf} u_m^{n0}}{2}, \quad (20)$$

$$G_s = \int_0^{u_m^{sf}} \sigma_s du_s = \frac{Ku_m^{sf} u_m^{s0}}{2}, \quad (21)$$

where  $u_m^{n0}$  ( $u_m^{s0}$ ) and  $u_m^{nf}$  ( $u_m^{sf}$ ) are the normal (shear) relative separation displacements corresponding to the damage initiation and ultimate failure under mixed-mode loading.

Based on equations (13) and (18):

$$u_m^{n0} = \frac{u_m^0}{\sqrt{1 + \beta^2}}, \quad (22)$$

$$u_m^{nf} = \frac{u_m^f}{\sqrt{1 + \beta^2}}, \quad (23)$$

$$u_m^{s0} = \frac{\beta u_m^0}{\sqrt{1 + \beta^2}}, \quad (24)$$

$$u_m^{sf} = \frac{\beta u_m^f}{\sqrt{1 + \beta^2}}. \quad (25)$$

Substituting equations (22)–(25) into (20) and (21),  $G_n$  and  $G_s$  can be established in terms of  $u_m^0$ ,  $u_m^f$  and  $\beta$  as:

$$G_n = \frac{Ku_m^0 u_m^f}{2(1 + \beta^2)}, \quad (26)$$

$$G_s = \frac{\beta^2 Ku_m^0 u_m^f}{2(1 + \beta^2)}. \quad (27)$$

Substituting equations (26) and (27) into the ultimate failure power law criterion equation (11), the mixed-mode delamination (complete debonding) relative separation displacement is obtained:

$$u_m^f = \begin{cases} \frac{2(1 + \beta^2)}{Ku_m^0} \left[ \left( \frac{1}{G_{nc}} \right)^\alpha + \left( \frac{\beta^2}{G_{sc}} \right)^\alpha \right]^{-1/\alpha} & u_n \geq 0 \\ u_s^f & u_n < 0 \end{cases}. \quad (28)$$

Note that as in (19), single-mode ultimate failure separations are included in equation (28). In particular, the normal mode criterion is obtained by setting  $\beta = 0$  to get  $u_m^f = u_n^f$ , and the shear model criterion by setting  $\beta = \infty$  to get  $u_m^f = u_s^f$ .

Similar to single-mode, to determine the loading and unloading conditions and track the current maximum separation displacement on the interface under mixed-mode loading, the variables  $u_m^{\max}$  are defined as:

$$u_m^{\max} = \max \{u_{m,\text{old}}^{\max}, u_m\}, \quad \text{with } u_m \geq 0, \quad (29)$$

where  $u_{m,\text{old}}^{\max}$  is the corresponding maximum mixed-mode separation displacement recorded from previous time step and is implemented in COMSOL as an algebraic equation in an ordinary differential equation (ODE) interface as:

$$u_{m,\text{old}}^{\max} = :u_m^{\max}. \quad (30)$$

The equality ‘=’ denotes that the left-hand side value is updated at the ‘tick’ of a new time step the ODE solver used in solving the ODE, which, in the present case is simply the algebraic equation (30).

For the mixed-mode loading condition, the constitutive equation of the CZM bilinear spring connection satisfies:

$$\sigma_m^p = \delta^{pq} K_m' u_m^q, \quad p, q = 1, 2, 3, \quad (31)$$

where the superscripts  $p$  and  $q$  each represent one of the three principal directions of the stress components of interfacial traction stresses,  $\sigma_m^p$  is the component in the  $p$  principal direction of the stress tensor and  $u_m^q$  is the relative displacement in the  $q$  direction, all under mixed-mode loading. Here  $\delta^{pq}$  is the Kronecker delta, defined as:

$$\delta^{pq} = \begin{cases} 1 & p = q \\ 0 & p \neq q \end{cases} \quad (32)$$

and  $K_m'$  is the updated penalty stiffness related to  $u_m^{\max}$  under

mixed-mode loading, expressed as:

$$K'_m = \begin{cases} K, & u_m^{\max} \leq u_m^0 \\ (1 - D_m)K + \frac{\langle -u_n \rangle}{-u_n} D_m K, & u_m^0 < u_m^{\max} < u_m^f, \quad u_n^{\max} \geq 0, \\ \frac{\langle -u_n \rangle}{-u_n} K, & u_m^{\max} \geq u_m^f \end{cases} \quad (33)$$

in which  $D_m$  is the damage evolution function under mixed-mode loading defined as:

$$D_m = \begin{cases} 0 & u_m^{\max} \leq u_m^0 \\ \frac{u_m^f(u_m^{\max} - u_m^0)}{u_m^{\max}(u_m^f - u_m^0)} & u_m^0 < u_m^{\max} < u_m^f, \quad u_n^{\max} \geq 0, \\ 1 & u_m^{\max} \geq u_m^f \end{cases} \quad (34)$$

Note that the normal penalty stiffness is applied to equation (33) when interpenetration is detected on the interface, i.e., when  $u_n < 0$ , (33) becomes:

$$K'_m = K, \quad \text{for } u_n < 0. \quad (35)$$

In a 3D/2D model, the constitutive equation (31) is implemented in weak form 'spring foundation' as a body force ( $\text{N m}^{-2}$ ) on the 2D thin films (surfaces  $k = 2, 3$  and 4 in figure 2) and as a boundary condition

$$\sigma \cdot \mathbf{n} = \sigma_m^p \quad (36)$$

on the bottom surface of the top stabilizer (surface  $k = 1$  in figure 2) and the top surface of the substrate (surface  $k = 5$  in figure 2). In a full-3D counterpart, the constitutive equation is implemented in weak form 'thin elastic layer' as an internal boundary condition (36) on the delamination interfaces (equivalent to interfaces  $k = 1 - 4$  in figure 2), each of which is a contact surface sandwiched between two connected 3D domains.

Note that since COMSOL (up to version 5.3a) has not yet implemented plasticity in the mechanical shell element [35], all 2D layers are implemented with the 2D membrane element, which includes plasticity but without bending stiffness. When modeling mechanical behavior in very thin and long plates, the membrane is a good approximation of the shell.

### 3. Simulation methodology

Delamination behavior in a REBCO conductor can be studied using transverse tensile stress, peel stress, shear stress and cleavage stress [14–23]. To study the generation and propagation of delamination in multiple directions,  $c$ -axis transverse tension (in the thickness direction) generated by an anvil is chosen as the load mode. The anvil is placed in the middle of the conductor's top surface with both its width and length smaller than the conductor's full width, as shown in in figure 3. Such an anvil load can generate a delamination propagating in both the longitudinal and width

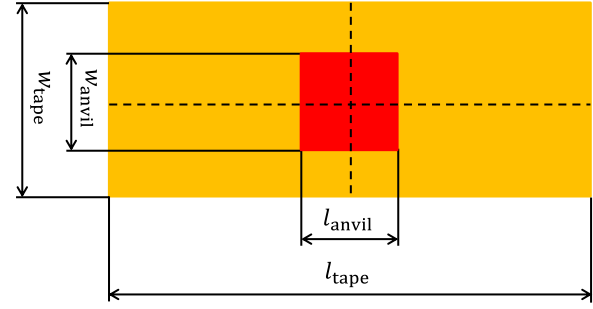


**Figure 3.** Size and position of the anvil and conductor. The yellow outer rectangle represents the top surface of the conductor, and the red center square is the anvil load section.

directions rather than solely in a single direction. The bottom of the conductor is fixed and an incrementally increasing upward displacement load is applied to the anvil to create delamination. Due to the spatial symmetry of the structure and boundary condition, only a quarter of the conductor is modeled. Isotropic elastoplastic material properties are defined for all the constituent layers. These are listed in table 1 for all constituent materials [11, 12]. Due to the lack of some data for the buffer, the elastoplastic material properties of the buffer are set to be the same as those of the REBCO. Experimental results showed that typical mechanical failures occur in a REBCO conductor in the form of cracks on the REBCO and/or buffer layers, or delamination at the interface between these two layers [15, 16]. This indicates that these are the weakest structures in the conductor. In view of this, all CZM delamination simulation results presented here, except those in section 4.6, focus only on the REBCO–buffer interface. According to available experimental results, it is found that the transverse tensile delamination strength, defined as the maximum transverse tensile stress at which delamination occurs, varies over a wide range between 10 and 110 MPa [14–19] and the delamination strength induced by shear stress (parallel to the conductor width direction) on the REBCO layer is about 30–60 MPa [23]. In simulation, the interfacial cohesive normal (tensile) strength  $\sigma_n^0$  and shear strength  $\sigma_s^0$  for the CZM on the REBCO–buffer interface (interface  $k = 3$  in figure 2) are chosen as  $\sigma^0 = \sigma_n^0 = \sigma_s^0 = 50$  MPa, which is within the range of published data. For simplicity, critical fracture energies release rates in the normal and shear directions were assumed to be the same with  $G_c = G_{nc} = G_{sc} = 10 \text{ J m}^{-2}$ , here the value is taken from [36]. The adjacent surfaces on the rest of the interfaces, i.e., interfaces  $k = 1, 2$ , and 4 in figure 2, are connected with spring connections without CZM's penalty stiffness degradation, i.e. the spring connection for these interfaces is simply  $\sigma = Ku$ . According to [37], the initial interface stiffness should be large enough to provide a reasonable stiffness yet small enough to reduce the risk of numerical instability, such reasonable value satisfies

$$K = \frac{aE_3}{t}, \quad (37)$$

where  $E_3$  is the through-thickness effective elastic property of the composite,  $t$  is the thickness of an adjacent

sub-laminate layer,  $a$  is a parameter much larger than 1 ( $a \gg 1$ ) so that the effective elastic properties of the composite will not be affected by the CZM cohesive surface. A high initial stiffness is used as  $K = 1 \times 10^6 \text{ N mm}^{-3}$  to meet the requirements listed above.

According to equations (1) and (2), the initial displacement at damage initiation separation is found to be  $u^0 = 50 \text{ nm}$ , and the ultimate failure separation at final failure  $u^f = 400 \text{ nm}$ , in both the normal and tangential directions.

#### 4. Results and discussions

The CZM delamination modeling theory on composite materials is well verified [30–33]. Here, it remains to verify and evaluate the 3D/2D modeling approach. It is, however, difficult to validate experimentally the 3D/2D delamination model because of large deviations in the published experimental results [16] and the lack of proper material properties for some of the layers and the interfaces between them, and particularly, the interface between the REBCO and buffer layers. As a result, a full-3D CZM model is developed to validate the 3D/2D mixed-dimensional CZM model. To avoid excessive computational efforts resulting from using extremely fine and a large number of meshes for the HAR 3D thin films, both the full-3D and 3D/2D models are built with a narrower width, with  $w_{\text{tape}} = 0.4 \text{ mm}$ , and a thicker buffer layer, increased from Superpower's  $0.2$  to  $0.5 \mu\text{m}$ . Moreover, to facilitate delamination to occur in the validating model, the side stabilizers are not included in either model. Since the scales of delamination separation and propagation are in the order of a micrometer, a short conductor length, with  $l_{\text{tape}} = 1 \text{ mm}$ , is sufficient for the study of delamination propagation and validation. The anvil is placed in the middle of the top surface with both its width and length equal to half of the width of the conductor, i.e.  $w_{\text{anvil}} = l_{\text{anvil}} = 0.2 \text{ mm}$ , as shown in figure 3.

##### 4.1. Delamination behavior in term of CZM

As all the results are based on the CZM model, the mechanisms and onset of delamination interpreted in term of CZM are first presented using the simulation results of the 3D/2D model. Figure 4(a) shows the displacements (relative to the original unstrained positions) of the REBCO and buffer layers at the symmetric center point (i.e., at center of the anvil in figure 3), where a delamination begins. The curves can be divided into three stages. In the first stage (a), the displacements of the REBCO and buffer layers increase with the increase of applied displacement load on the anvil in the transverse direction until the separation between the REBCO and buffer layers reaches the critical damage initiation separation  $u_m^0$ . After that, in stage (b), the displacement of the REBCO layer increases with a slightly steeper slope, while that of the buffer layer drops gradually to zero. When the displacement between the REBCO and buffer layers reaches the ultimate failure separation  $u_m^f$ , delamination on the

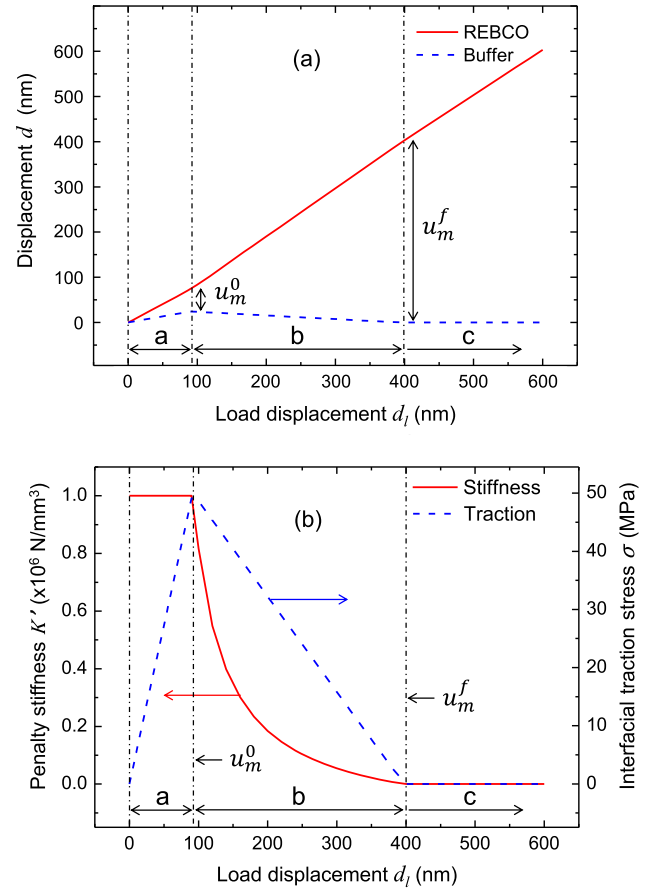


**Figure 4.** (a) Displacement versus applied load displacement in the REBCO and buffer layers. (b) Penalty stiffness and interfacial traction stress versus applied load displacement. The damage and delamination onset points are included.

interface occurs in stage (c). Note that during delamination, there is no separation on the buffer layer and the REBCO layer increases linearly with the increase of applied load. The generation of delamination can be further understood from the aspects of stiffness and interfacial traction stress, as shown in figure 4(b). In stage (a), a high initial stiffness is used to hold the two surfaces across the interface together and the interfacial traction stress (calculated by equation (31)) increases linearly in the elastic range. When the interfacial traction attains the first critical strengths at  $u_m^0$ , damage onset is produced but no delamination occurs yet on the interface. In stage (b), the penalty stiffness  $K'$  reduces to zero gradually and nonlinearly while the interfacial traction stress reduces to zero linearly. In stage (c), both the stiffness and interfacial traction stress become zero, indicating that no cohesion binding force exists between the REBCO and buffer layers and thus delamination occurs.

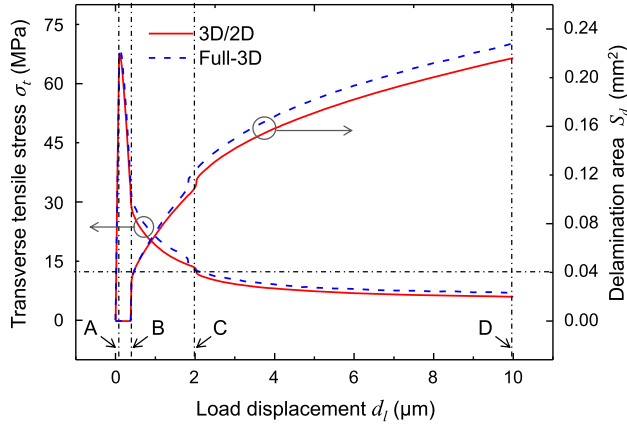
##### 4.2. Computational validation

**4.2.1. Validation at the conductor level.** Figure 5 compares the results for transverse tensile stress and delamination area obtained from the same 3D/2D model (figure 4) and the full-3D counterpart at the conductor level under the same anvil



**Table 1.** Materials properties of all the constituent materials of the REBCO conductor.

	Thickness ( $\mu\text{m}$ )	Young's modulus $E$ (GPa)	Poisson's ratio $\nu$	Yield strength $\sigma_y$ (MPa)	Tangent modulus $E_t$ (GPa)
Copper	20 + 20	70	0.343	120	5
Silver	2	76	0.37	65	4
REBCO	1	157	0.3	700	5
Buffer	0.5	157	0.3	700	5
Hastelloy	50	170	0.307	980	6

**Figure 5.** Applied transverse tensile stress and delamination area versus applied load displacement in 3D/2D and full-3D models.

load used for figure 4. Here, the applied transverse tensile stress is defined as applied external transverse force  $F_e$  divided by anvil area; this method has been used to determine delamination strength experimentally [14, 16, 17, 19]. Using the 3D/2D results as an example, the applied transverse tensile stress first increases sharply to the maximum value when the applied load displacement reaches the first critical load condition at load displacement A at around  $0.09 \mu\text{m}$ , which is equal to  $u_m^0$  in figure 4, signifying the onset of damage. The applied transverse tensile stress then drops sharply until the load displacement reaches another critical load condition at load displacement B at around  $0.4 \mu\text{m}$ , which is equal to  $u_m^f$  in figure 4, signifying the onset of delamination. Note that at displacement B, i.e. at  $u_m^f$ , the interfacial traction stress is zero (figure 4(b)) while the applied transverse tensile stress is  $\sim 28 \text{ MPa}$ . Until this point, no real delamination occurs, as seen from the zero value on the curve representing the delamination area on the interface between the REBCO and buffer layers. The deformations (in displacements magnified at  $10\times$ ) on different layers of the 3D/2D conductor at the instances around load displacements A–D (marked in figure 5) can also be seen in figures 6(a)–(d). At load displacement A, both the interfacial traction (figure 4(b)) and applied transverse tensile stresses reach their maximum values, however, no delamination occurs yet, as seen in figure 6(a). A slight increase in load displacement beyond B causes the delamination area to jump abruptly to a special value,  $S_d = 0.04 \text{ mm}^2$ , which is the anvil section area, signifying the occurrence of delamination, as seen in figure 6(b). As the load displacement further increases, the

transverse tensile stress decreases gradually and the delamination propagates along both the longitudinal and width directions until it reaches the edges (across the width) of the conductor at load displacement C at about  $2 \mu\text{m}$ , as seen in figure 6(c). The onset of the edge-to-edge delamination across the conductor width at C causes the inflection points in both the applied transverse tensile stress and delamination area in figure 5. As the load displacement increases beyond C, the edge-to-edge delamination propagates along the length of the conductor, as seen in figure 6(d), and the applied transverse tensile stress becomes almost independent of the applied displacement. Note that in figure 6(d) that although the delamination occurs on the interface between the REBCO and buffer layers, there are visible separations between the top copper and the silver layers and the silver and REBCO layers, but there is no visible separation between the buffer and the Hastelloy layers. This is because the buffer layer is bonded with Hastelloy, which hardly deforms, and there is no interfacial traction force on the REBCO–buffer interface once delamination occurs (beyond  $u_m^f$  in figure 4(b)).

The same delamination generation and propagation processes seen in figure 6 can be further observed from the delaminated surface on the REBCO–buffer interface as represented by the red–brown regions, which grow from the lower right corner, as shown in figure 7. Figure 7(a) shows that no delamination occurs at load displacement A. The delamination starts from the anvil section at a load displacement slightly greater than B, as shown in figure 7(b). When the load displacement increases beyond B, the delamination propagates radially until it reaches the edges across the conductor width at load displacement C, as shown in figure 7(c). After that, the conductor-wide delamination propagates longitudinally, as shown in figure 7(d). Hereafter, such a conductor-wide delamination is referred as a peeling process. It is clear from figure 7 that for load displacement larger than C, the conductor is experiencing a peeling process.

During the entire delamination process the system satisfies the energy balance equation:

$$E_{\text{sys}} = E_{\text{del}} + E_{\text{str}}, \quad (38)$$

where  $E_{\text{sys}}$  is the energy of the entire system, the value of which is equal to the work done by an external transverse force  $F_e$ , i.e.  $E_{\text{sys}} = F_e d_l$ , where  $d_l$  is the load displacement.  $E_{\text{del}}$  and  $E_{\text{str}}$  represent the release energy induced by delamination and the strain energy, respectively.  $E_{\text{del}}$  is determined by the CZM parameter  $G_c$  which is used with the same value

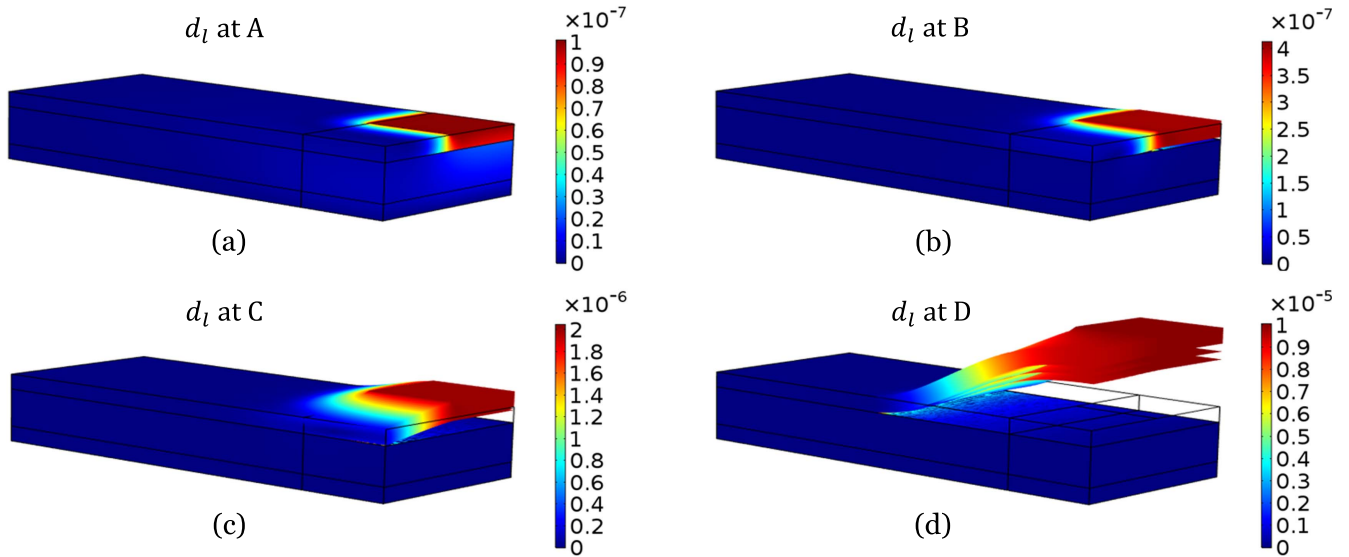


**Figure 6.** Deformations (as displacements magnified 10 $\times$ ) in the 3D/2D model observed at load displacements A, B, C, and D marked in figure 5. A symmetrical quarter of the conductor is shown.

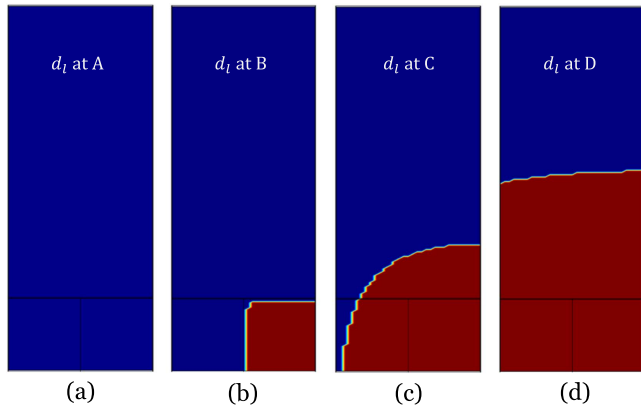


**Figure 7.** Delaminated surfaces on the REBCO–buffer interface of the 3D/2D model as observed at load displacements A, B, C, and D marked in figure 5. The red–brown lower right regions represent the delaminated regions. A symmetrical quarter of the conductor is shown.

in both the 3D/2D and full-3D models, and  $E_{str}$  is a function of stress and strain. As remarked above, membrane elements instead of shell elements are used in modeling the silver, REBCO, and buffer layers in the 3D/2D model. Since a membrane element does not have any bending stiffness [35], the stresses in the silver, REBCO and buffer layers in the 3D/2D model are smaller than that in full-3D model under the same deformation condition. This results in smaller strain energy and smaller external force. As a result, the applied transverse tensile stress during the peeling process in the 3D/2D model is slightly smaller than that in the full-3D model, as shown in figure 5.

Figure 5 also shows that the delamination area in the 3D/2D model is slightly smaller and the inflection points in the 3D/2D curves appear slightly later than those of the full-3D model. These results tell that the same load displacement causes slightly larger and faster delamination propagation in the full-3D model than in the 3D/2D model. These

discrepancies are mainly the consequences of the lacking of bending stiffness in membrane elements—besides experiencing smaller stresses, the membrane-based layers are also softer to bend in the 3D/2D model than in the full-3D model, resulting in weaker and thus slower delamination. However, since the silver, REBCO, and buffer layers are thin enough for the membranes to be good approximations of shells, the errors in the 3D/2D model are all within 5% when measured at  $d_l = 10 \mu\text{m}$  (displacement D in figure 5), which is considered to be an error in this study.

**4.2.2. Validation at the constituent layer level.** Figure 8 compares the stress distributions on the major constituent layers in the same 3D/2D and full-3D counterpart models (used for figures 4–7) when the load displacement reaches  $d_l = 10 \mu\text{m}$  under the same anvil load. The stress distributions are taken along the conductor center (i.e., on the longitudinal symmetry axis) at the bottom surface of the top copper layer (surface  $k = 1$  in figure 2), the surfaces of the silver, REBCO, and buffer layers layer (surface  $k = 2, 3$  and 4, respectively), and the top surface of the Hastelloy layer (surface  $k = 5$ ). The REBCO layer experiences the largest stress variation, changing from a compressive stress of about  $-900 \text{ MPa}$  at  $l_p \sim 0.1 \text{ mm}$ , which is located at the anvil's edge, to a tensile stress of about  $820 \text{ MPa}$  at  $l_p \sim 0.3 \text{ mm}$ , which is near the locations of the crack (delamination) fronts in both models. Here  $l_p$  is the distance from the symmetric end of the half-length conductor. In contrast, the buffer layer, which is thinner but has the same material properties as the REBCO in calculation, has almost no stress variation except at the crack front ( $l_p \sim 0.3 \text{ mm}$ ). This phenomenon indicates that the delamination occurs between the REBCO and buffer layers, and is consistent with the results observed in figures 4–7. All other layers above the delaminated interface, i.e., the top copper and silver layers, also experience two stress concentration regions at the same locations as on the REBCO layer, but

with much smaller magnitudes. It can also be seen that plastic deformation (decreased slope) occurs on the REBCO layer near the anvil edge and from  $l_p \sim 0.2$  mm to the crack front. In the 3D/2D and full-3D models, the onset of a plastic deformation is used to represent the occurrence of fracture in the brittle layers which include the REBCO and buffer layers. Therefore, the plastic deformations on the REBCO layer means irreversible damage has occurred near the anvil edge and crack front, which would induce irreversible degradation in critical current. Although figure 6 shows that there is no visible deformation on the bonded buffer and Hastelloy layers, the shear stress generated by the large deformation on the delaminated REBCO layer still induces a stress concentration on these two layers at the crack front. Table 2 records the stresses and positions at the crack fronts obtained from the full-3D and 3D/2D models and the numerical errors in the 3D/2D model when compared to the full-3D counterpart. As compared to the results of the 3D/2D model, the stress variations (e.g., compressive-tensile transition and crack front location) in the full-3D model occur slightly sooner, and thus farther from the delamination initiation position, as seen in figure 8 and table 2. This reflects that the lack of bending stiffness on the membranes causes delamination on the REBCO-buffer interface to propagate slightly slower in the 3D/2D model than in the full-3D model under the same load displacement.

#### 4.3. Efficiency of the 3D/2D model

It is difficult to simulate a model composed of a HAR thin film in 3D with mesh-based numerical methods such as FEM due to the enormous number of degrees of freedom (DoFs) required for fine meshing, and in general, the smaller time steps for a time-dependent problem. The delamination model studied here is composed of three laminated HAR thin films, exacerbating the HAR modeling challenge. The 3D/2D model avoids the difficulties of fine meshing by modeling the HAR thin films as 2D layers. The consequences are that the meshes and time steps are now independent of the thicknesses of the thin films. In the study here, a convergent 3D/2D delamination model requires about  $5.5 \times$  less DoFs and runs about  $20 \times$  faster while maintaining sufficient accuracy, as shown in table 2, when compared to a full-3D counterpart with comparable mesh densities on the 3D domains. Table 3 details the actual DoFs and computational times used in the 3D/2D model and the full-3D counterpart. This efficiency gain is mainly due to the vast reduction in the DoFs and the replacement of thin 3D solid elements by easier-to-compute 2D surface elements.

#### 4.4. Effect of anvil size

Figure 9 illustrates the effects of anvil length on the applied transverse tensile stress and applied force required to generate delamination in the 3D/2D model. The width of the anvil is

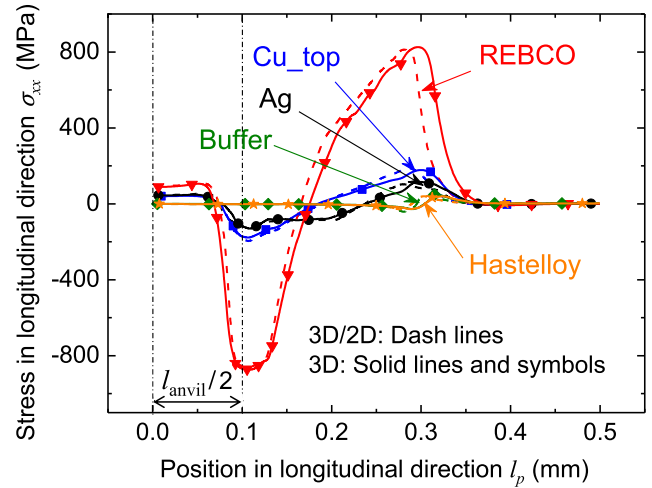


**Figure 8.** Stress distributions on different constituent layers of the 3D/2D and full-3D models. Stresses are measured along the conductor center in the longitudinal direction when the load displacement  $d_l = 10 \mu\text{m}$ . Half of the conductor length is shown. Vertical dashed-dotted lines show the position and size of the symmetrical half of the anvil.

chosen here to be the same as the conductor width used in the validation model (i.e.,  $w_{\text{anvil}} = w_{\text{tape}} = 0.4$  mm) such that the effects of delamination propagation in the width direction are negligible. Delamination under this condition becomes a peeling process. The anvil length varies from 0.2 to 8 mm and the conductor length is always 1.5 times the anvil length. The applied transverse tensile stress decreases with increasing anvil length, as shown in figure 9(a). Moreover, the longer the anvil, the closer the stress's peak (at  $u_m^0 \sim 0.09 \mu\text{m}$ ) is to the interfacial cohesive normal strength  $\sigma_n^0 = 50$  MPa, which is defined in the CZM. This is because when a delamination occurs under a transverse tensile load, not only the cohesive binding under the anvil section resists delamination but also the elastoplastic deformation at the crack (delamination) front contributes to the delamination strength. The normal cohesive binding force is proportional to the anvil area (as interfacial traction normal stress multiplied by anvil area) while the normal force due to the elastoplastic deformation is proportional to the total length of the crack fronts, here equal to  $2 \times w_{\text{anvil}} = 2 \times w_{\text{tape}}$ , and is independent of the anvil length. As a result, the longer the anvil, the larger the ratio of the contribution of the cohesive binding force to the force due to elastoplastic deformation in the delamination process. In other words, the shorter the anvil, the greater the effect of the elastoplastic deformation to the transverse tension as compared to the diminishing effect of the CZM cohesive zone. A larger anvil, therefore, requires larger applied transverse force, as shown in figure 9(b), but results in smaller transverse tensile stress ( $\sigma_t$ ) that is closer to  $\sigma_n^0$ . In contrast, a smaller anvil results in larger  $\sigma_t$  throughout the entire damage-delamination process (recall that  $\sigma_t$  is defined as the applied transverse force divided by the anvil area), as shown in

**Table 2.** Crack front stresses and positions on all the constituent layers of the full-3D and 3D/2D models, and maximum errors in the 3D/2D model as compared to the full-3D model, as measured from figure 8.

	Layer	3D	3D/2D	Absolute error (MPa or mm)	Relative error (%)
Stress at crack front (MPa)	Cu_top	183	188	5	2.73
	Ag	115	103	−12	−10.43
	YBCO	827	812	−15	−1.81
	Buffer	47	46	−1	−2.13
	Hastelloy	39	40	1	−2.5
Crack front position (mm)		0.300	0.285	−0.015	−5.00

**Table 3.** DoFs and computational times used in full-3D and 3D/2D models.

	3D	3D/2D
DoFs	198 871	36 462
Computational time	22 h 56 min	1 h 10 min

figure 9(a). Without the elastoplastic deformation effect, the maximum of  $\sigma_t$  is equal to  $\sigma_n^0$ .

Notice in figure 9(b) that the applied transverse forces in the peeling process (at  $d_l > 0.4 \mu\text{m}$ ), are around 0.57 N. Recall that during delamination (for  $d_l > 0.4 \mu\text{m}$  in figure 4(b)), there is no cohesion binding force exists between the REBCO and buffer layers and thus the applied transverse force at this stage is purely peeling force. The peel force per unit width (the interfacial fracture energy per unit area) can be written as [21]:

$$F_p = \gamma + \varphi, \quad (39)$$

where  $\gamma$  is the debonding energy and  $\varphi$  is the work expenditure rate per unit advance of the peel propagation (i.e., work dissipation) caused by plastic deformation in the adherent. During the peeling process,  $\gamma$  and  $\varphi$  are almost the same for different anvil lengths under the same applied displacement load.

Another effect of anvil size is reflected by the anvil width, as shown in figure 10. The ratio between the anvil width and conductor width, i.e.,  $w_{\text{anvil}}/w_{\text{tape}}$ , varies from 0.25 to 1 with  $w_{\text{tape}} = 0.4 \text{ mm}$ ,  $l_{\text{tape}} = 1 \text{ mm}$  and  $l_{\text{anvil}} = 0.2 \text{ mm}$ . It can be seen that the applied transverse tensile stress increases with decreasing anvil width for the same reasons as the anvil length effects. The same observation of anvil width effect is reported in [17]. Note that for all  $w_{\text{anvil}}/w_{\text{tape}} < 1$  cases, an inflection point in the transverse tensile stress (as seen in figure 5) is created when the delamination reaches the edges across the conductor width.

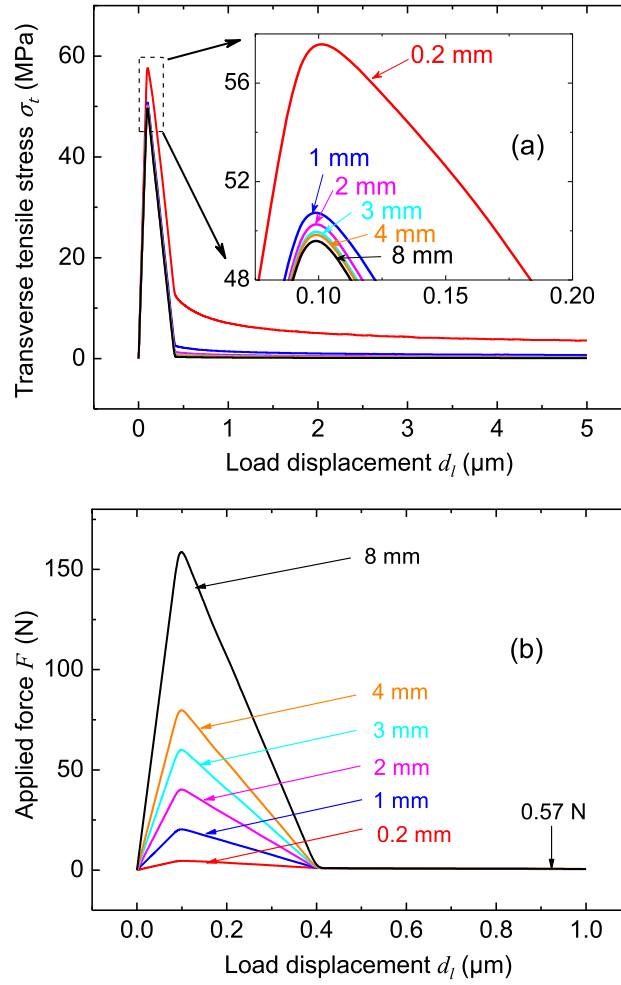
#### 4.5. Effect of initial crack

Figure 11 shows the effect of pre-crack length on the delamination behavior. The width and length of the anvil are chosen to be the same as the conductor width used in the validation model (i.e.,  $w_{\text{anvil}} = l_{\text{anvil}} = w_{\text{tape}} = 0.4 \text{ mm}$ ), and the conductor length is  $l_{\text{tape}} = 1 \text{ mm}$ . The pre-cracks are located on the REBCO–buffer interface symmetrically under the center of the anvil and run across the entire width of the conductor with the ratio of pre-crack length to anvil length, i.e.,  $l_{\text{pre}}/l_{\text{anvil}}$ , varying from 0.25 to 1. The curves can be

divided into two stages: debonding and peeling. In the first stage, the larger the pre-crack, the smaller the peak of the transverse tensile stress. After the peaks, the stresses in all cases decrease to  $\sim 12 \text{ MPa}$ , and the peeling process starts. In the debonding process, the system satisfies the energy balance equation (38).  $E_{\text{del}}$  increases linearly with the no-pre-crack anvil section area while  $E_{\text{str}}$  is independent of the pre-crack and only related to energy dissipation due to deformations, including those from elastic and plastic contributions. Therefore, the applied transverse force decreases with increasing pre-crack area. Note that since  $\sigma_t$  is defined as the applied transverse force divided by the anvil area, which is fixed here regardless of the pre-crack size,  $\sigma_t$  shown in figure 11 also decreases with increasing pre-crack area, whereas  $\sigma_t$  in figures 9 and 10 increases with decreasing anvil size (either in length or width). In the peeling process, equation (39) is satisfied; both the debonding energy and work expenditure rate due to plastic deformation in the adherent parts are independent of the pre-crack length. As a result, the peeling forces, and thus  $\sigma_t$ , are the same regardless of the pre-crack length. The dependence of the applied force on the crack size may explain why the delamination strength obtained in experimental peel tests varies widely from test to test, even for samples cut from the same conductor. For example, it is reported that the  $c$ -axis failure/delamination stress obtained from the same pin-pull transverse tension experiment varies from 10 to 110 MPa [16]. As a REBCO conductor is a laminated composite and REBCO itself is brittle, it is likely that some defects exist on the REBCO layer or at the REBCO/buffer layers interface. As a result, smaller delamination strength will be observed from a transverse load test applied on a conductor with large defects, such as cracks, included within the loaded section than on one with smaller defects.

#### 4.6. Multi-interface with CZM

The results presented before are based on a CZM defined on the REBCO–buffer interface  $k = 3$  (figure 2). Experimental results showed that delamination could occur on any interface with the weakest delamination strength, which is dictated by the CZM parameters and stress/strain evolutions at the interfaces. Here, the conductor and anvil configurations are the same as those used for figure 8, but now all the interfaces ( $k = 1\text{--}4$  in figure 2) are implemented with CZM and the weakest delamination strength is set on one chosen interface.



**Figure 9.** Applied transverse tensile stress and force versus applied load displacement for different anvil lengths, (a) applied transverse tensile stresses and (b) applied forces.

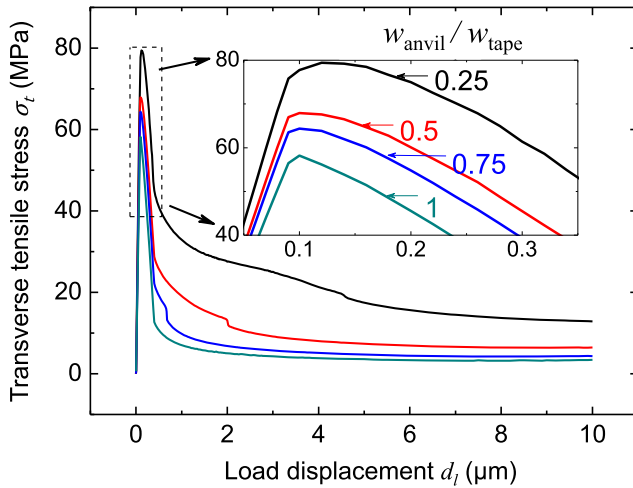


**Figure 10.** Applied transverse tensile stress versus applied load displacement with different anvil widths in terms of ratio  $w_{\text{anvil}}/w_{\text{tape}}$ .

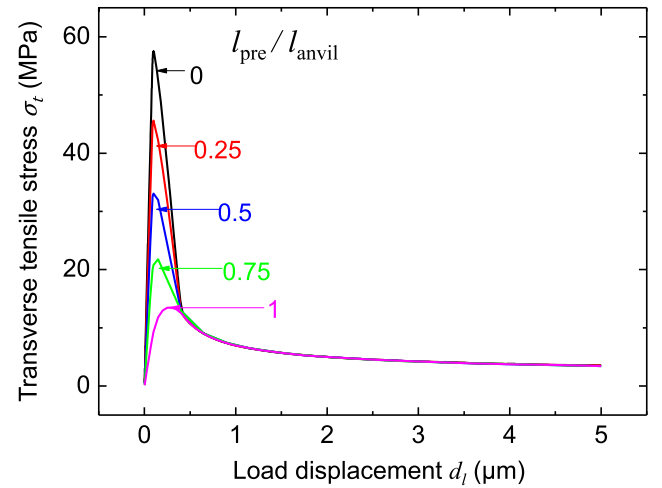


**Figure 11.** Applied transverse tensile stress versus applied load displacement with different pre-crack sizes in terms of ratio  $l_{\text{pre}}/l_{\text{anvil}}$ .

More specifically, the weakest delamination strength is created by using the smallest normal and shear strengths ( $\sigma_n^0$  and  $\sigma_s^0$ ) and critical fracture energy release rates in the normal and

shear directions ( $G_{nc}$  and  $G_{sc}$ ). Four cases are studied. In Case I, the weakest delamination strength is set on interface  $k = 1$ , between the top copper and silver layers, in Case II on



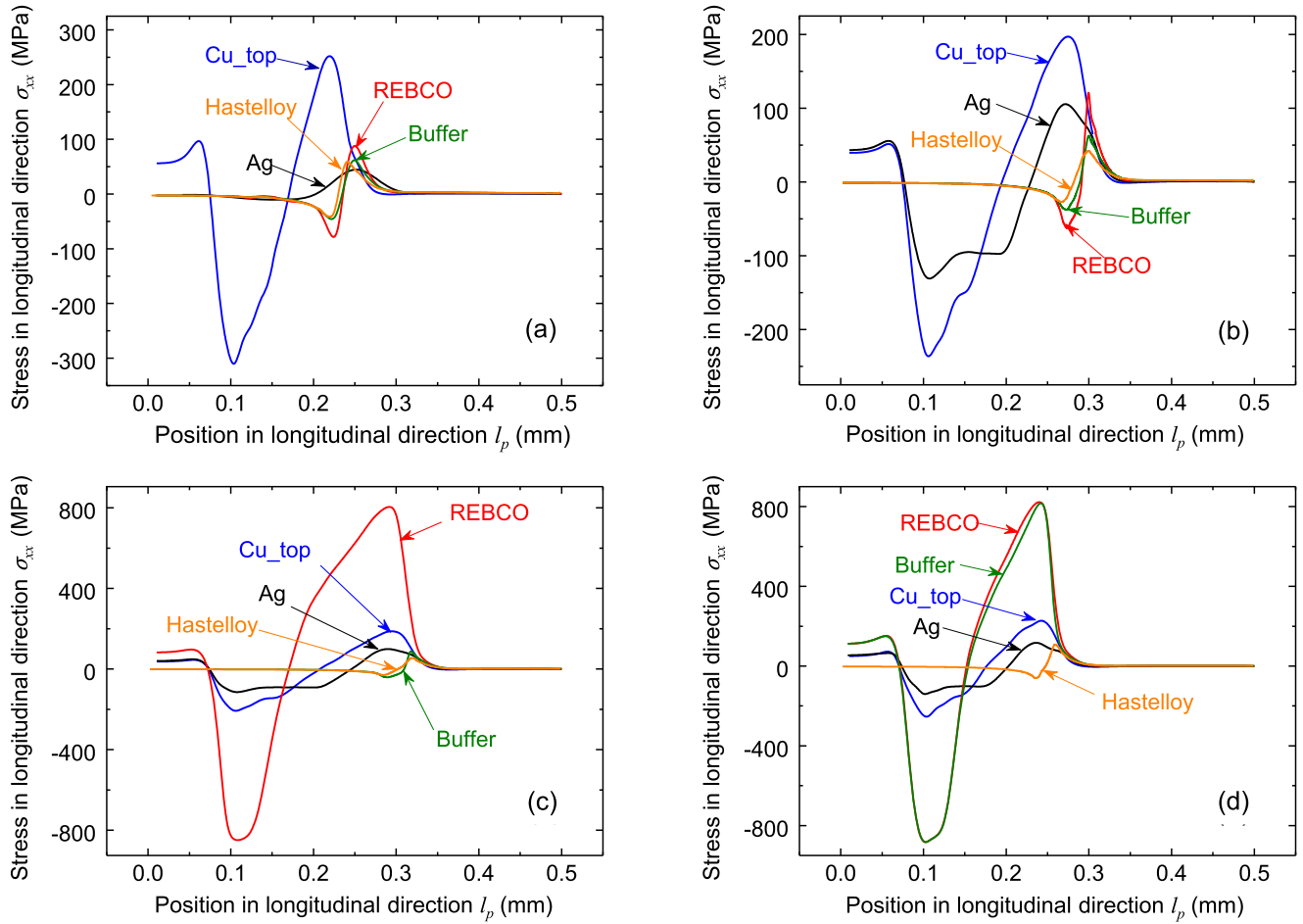


**Figure 12.** Stress distributions on each constituent layer with the weakest CZM parameters located: (a) Case I, on interface  $k = 1$ , (b) Case II, on interface  $k = 2$ , (c) Case III, on interface  $k = 3$ , and (d) Case IV, on interface  $k = 4$ . Half of the conductor length is shown.

interface  $k = 2$ , between the silver and REBCO layers, in Case III on interface  $k = 3$ , between REBCO and buffer layers and in Case IV on interface  $k = 4$ , between the buffer and Hastelloy layers. For example, in Case I on the interface  $k = 1$  the parameters are chosen as  $\sigma_n^0 = \sigma_s^0 = 50$  MPa and  $G_{nc} = G_{sc} = 10$  J m<sup>-2</sup>, while on all the other interfaces the parameters are  $\sigma_n^0 = \sigma_s^0 = 500$  MPa and  $G_{nc} = G_{sc} = 1000$  J m<sup>-2</sup>. Under the same anvil transverse tension pull (recall that the bottom of the conductor is fixed), the stress distributions on each constituent layers for the four cases are shown in figure 12. It can be seen that in all cases, delamination occurs on the interface with the weakest delamination strength, with stress distributions similar to those seen in figure 8. In each case, the layer or layers above the delamination interface have two stress concentration regions, one located near the anvil edge (e.g., near position at 0.1 mm in figure 12(a)), and the other is located near the crack front (e.g., near position at 0.22 mm in figure 12(a)). On the layer or layers below the delamination interface, there is only one stress concentration region located near the crack front, which is due to the shear stress caused by the layers ‘being pulled’ above the delamination interfaces. It can be seen by comparing the 3D/2D result in figure 8 (with CZM on interface  $k = 3$ ) and the result in figure 12(c) that the stress

distributions on all layers are almost the same. These results show that regardless whether the other interfaces are implemented with CZM or not, the delamination behavior and stress distributions on the interface are determined by the CZM on the weakest interface. This justifies the simulation approach mentioned in section 3 that if the weakest interface is known in advance, using only the CZM parameters on the weakest interface is acceptable for simulating the delamination behavior in a REBCO conductor.

## 5. Conclusion

An elastoplastic FEM delamination model based on CZM is built to study the delamination behaviors in REBCO conductors. A 3D/2D mixed-dimensional method is used to overcome the meshing difficulties commonly encountered in modeling laminated thin film multilayers in full-3D FEM models. The mixed-dimensional modeling approach allows all major constituent layers of a coated conductor tape to be included and modeled in real dimensions. It also makes computation much more efficient in 3D/2D models than in the full-3D counterparts.

Results show that the smaller the anvil size, the larger the applied transverse tensile stress needed to cause delamination, consistent with the experimental observations. In addition, simulations with different pre-crack sizes explain why experimental results on delamination strength usually have large discrepancies. Stress distributions of all the constituent layers in a REBCO conductor under different delamination sites are predicted. Results indicate that the layers above the delamination interface experience two stress concentration regions, one located near the anvil edges, and the other near the crack front. In contrast, only one stress concentration region, located near the crack front, is seen on the layers below the delamination interface; this is due to the shear stress caused by the layers above the delamination interface.

Large-scale, complicated coil models with delamination modeling can be built upon the bases of the conductor tape delamination model and its 3D/2D modeling techniques. The 3D/2D modeling techniques provide a general modeling methodology for coupling other physics, such as thermal and electric, for modeling of delamination induced, for example, by thermal expansion mismatch due to cooling and quench. The general modeling methodology can also be applied to composite models comprised of any number of laminated HAR thin layers.

## Acknowledgments

P F Gao would like to thank the financial support of ‘Chinese Top University Graduate Students Studying Abroad’ program, Chinese Scholarship Council No. 201506180066. P F Gao and X Z Wang would like to thank the support of the National Natural Science Foundation of China (11672120).

## ORCID iDs

Wan-Kan Chan  <https://orcid.org/0000-0001-5936-8537>  
Justin Schwartz  <https://orcid.org/0000-0002-7590-240X>

## References

- [1] Schwartz J *et al* 2008 High field superconducting solenoids via high temperature superconductors *IEEE Trans. Appl. Supercond.* **18** 70–81
- [2] Markiewicz W D, Miller J R, Schwartz J, Trociewitz U P and Weijers H W 2006 Perspective on a superconducting 30 T/1.3 GHz NMR spectrometer magnet *IEEE Trans. Appl. Supercond.* **16** 1523–6
- [3] Schwartz J, Hunte F, Chan W, Gou X, Liu X, Phillips M, Le Q, Naderi G, Turenne M and Ye L 2011 Status of high temperature superconductor based magnets and the conductors they depend upon *Eur. Supercond. News Forum* **16** ST262
- [4] Senatore C, Alessandrini M, Lucarelli A, Tediosi R, Uglietti D and Iwasa Y 2014 Progresses and challenges in the development of high-field solenoidal magnets based on RE123 coated conductors *Supercond. Sci. Technol.* **27** 103001
- [5] Sorbom B N *et al* 2015 ARC: a compact, high-field, fusion nuclear science facility and demonstration power plant with demountable magnets *Fusion Eng. Des.* **100** 378–405
- [6] Ito S, Yusa N, Yanagi N, Tamura H, Sagara A and Hashizume H 2016 Mechanical and electrical characteristics of a bridge-type mechanical lap joint of HTS STARS conductors *IEEE Trans. Appl. Supercond.* **26** 4201510
- [7] Miyazaki H, Iwai S, Tosaka T, Tasaki K and Ishii Y 2014 Degradation-free impregnated YBCO pancake coils by decreasing radial stress in the windings and method for evaluating delamination strength of YBCO-coated conductors *IEEE Trans. Appl. Supercond.* **24** 4600905
- [8] Miyazaki H, Iwai S, Tosaka T, Tasaki K and Ishii Y 2015 Delamination strengths of different types of REBCO-coated conductors and method for reducing radial thermal stresses of impregnated REBCO pancake coils *IEEE Trans. Appl. Supercond.* **25** 6602305
- [9] Iwasa Y, Bascunan J, Hahn S, Tomita M and Yao W J 2010 High-temperature superconducting magnets for NMR and MRI: R&D activities at the MIT Francis Bitter Magnet Laboratory *IEEE Trans. Appl. Supercond.* **20** 718–21
- [10] Guan M, Hahn S, Bascuñán J, Wang X, Gao P, Zhou Y and Iwasa Y 2016 A parametric study on overband radial build for a REBCO 800 MHz insert of a 1.3 GHz LTS/HTS NMR magnet *IEEE Trans. Appl. Supercond.* **26** 4301205
- [11] Osamura K, Sugano M, Machiya S, Adachi H, Ochiai S and Sato M 2009 Internal residual strain and critical current maximum of a surrounded Cu stabilized YBCO coated conductor *Supercond. Sci. Technol.* **22** 065001
- [12] Zhang Y, Hazelton D, Kelley R, Kasahara M, Nakasaki R, Sakamoto H and Polyanskii A 2016 Stress–strain relationship, critical strain (stress) and irreversible strain (stress) of IBAD-MOCVD-based 2G HTS wires under uniaxial tension *IEEE Trans. Appl. Supercond.* **26** 8400406
- [13] Otsuka A, Kiyoshi T and Takeda M 2010 A 1.3 GHz NMR magnet design under high hoop stress condition *IEEE Trans. Appl. Supercond.* **20** 596–9
- [14] van der Laan D C, Ekin J W, Clickner C C and Stauffer T C 2007 Delamination strength of YBCO coated conductors under transverse tensile stress *Supercond. Sci. Technol.* **20** 765–70
- [15] Takematsu T, Hu R, Takao T, Yanagisawa Y, Nakagome H, Uglietti D, Kiyoshi T, Takahashi M and Maeda H 2010 Degradation of the performance of a YBCO-coated conductor double pancake coil due to epoxy impregnation *Physica C* **470** 674–7
- [16] Majkic G, Galstyan E, Zhang Y F and Selvamanickam V 2013 Investigation of delamination mechanisms in IBAD-MOCVD REBCO coated conductors *IEEE Trans. Appl. Supercond.* **23** 6600205
- [17] Shin H S and Gorospe A 2014 Characterization of transverse tensile stress response of critical current and delamination behaviour in GdBCO coated conductor tapes by anvil test *Supercond. Sci. Technol.* **27** 025001
- [18] Dizon J R C, Gorospe A B and Shin H S 2014 Numerical analysis of stress distribution in Cu-stabilized GdBCO CC tapes during anvil tests for the evaluation of transverse delamination strength *Supercond. Sci. Technol.* **27** 055023
- [19] Liu W, Zhang X Y, Zhou J and Zhou Y H 2015 Delamination strength of the soldered joint in YBCO coated conductors and its enhancement *IEEE Trans. Appl. Supercond.* **25** 6606109
- [20] Zhang Y *et al* 2012 Adhesion strength study of IBAD-MOCVD-based 2G HTS wire using a peel test *Physica C* **473** 41–7
- [21] Kesgin I, Khatri N, Liu Y H, Delgado L, Galstyan E and Selvamanickam V 2016 Influence of superconductor film composition on adhesion strength of coated conductors *Supercond. Sci. Technol.* **29** 015003

- [22] Yanagisawa Y, Nakagome H, Takematsu T, Takao T, Sato N, Takahashi M and Maeda H 2011 Remarkable weakness against cleavage stress for YBCO-coated conductors and its effect on the YBCO coil performance *Physica C* **471** 480–5
- [23] Liu L Y, Zhu Y P, Yang X S, Qiu T and Zhao Y 2016 Delamination properties of YBCO tapes under shear stress along the width direction *IEEE Trans. Appl. Supercond.* **26** 6603406
- [24] Chan W K, Masson P J, Luongo C A and Schwartz J 2009 Influence of inter-layer contact resistances on quench propagation in  $\text{YBa}_2\text{Cu}_3\text{O}_{7-x}$  coated conductors *IEEE Trans. Appl. Supercond.* **19** 2490–5
- [25] Chan W K, Masson P J, Luongo C and Schwartz J 2010 Three-dimensional micrometer-scale modeling of quenching in high-aspect-ratio  $\text{YBa}_2\text{Cu}_3\text{O}_{7-\delta}$  coated conductor tapes: I. Model development and validation *IEEE Trans. Appl. Supercond.* **20** 2370–80
- [26] Chan W K and Schwartz J 2011 Three-dimensional micrometer-scale modeling of quenching in high-aspect-ratio  $\text{YBa}_2\text{Cu}_3\text{O}_{7-\delta}$  coated conductor tapes: II. Influence of geometric and material properties and implications for conductor engineering and magnet design *IEEE Trans. Appl. Supercond.* **21** 3628–34
- [27] Chan W K and Schwartz J 2012 A hierarchical three-dimensional multiscale electro-magneto-thermal model of quenching in  $\text{REBa}_2\text{Cu}_3\text{O}_{7-\delta}$  coated-conductor-based coils *IEEE Trans. Appl. Supercond.* **22** 4706010
- [28] Hillerborg A, Mod  er M and Petersson P-E 1976 Analysis of crack formation and crack growth in concrete by means of fracture mechanics and finite elements *Cement Concr. Res.* **6** 773–81
- [29] Camanho P P, Davila C G and de Moura M F 2003 Numerical simulation of mixed-mode progressive delamination in composite materials *J. Compos. Mater.* **37** 1415–38
- [30] Turon A, Camanho P P, Costa J and Renart J 2010 Accurate simulation of delamination growth under mixed-mode loading using cohesive elements: definition of interlaminar strengths and elastic stiffness *Compos. Struct.* **92** 1857–64
- [31] Zhu W, Yang L, Guo J W, Zhou Y C and Lu C 2015 Determination of interfacial adhesion energies of thermal barrier coatings by compression test combined with a cohesive zone finite element model *Int. J. Plast.* **64** 76–87
- [32] Xu Q, Tao W M, Qu S X and Yang Q D 2015 A cohesive zone model for the elevated temperature interfacial debonding and frictional sliding behavior *Compos. Sci. Technol.* **110** 45–52
- [33] Nourani A, Akbari S and Spelt J K 2016 Fracture load prediction of BGA solder joints: cohesive zone modeling and experimental verification *Int. J. Solids Struct.* **90** 30–44
- [34] Cui W C, Wisnom M R and Jones M 1992 A comparison of failure criteria to predict delamination of unidirectional glass epoxy specimens waisted through the thickness *Composites* **23** 158–66
- [35] COMSOL 2017 *COMSOL Multiphysics Structural Mechanics Module User's Guide Version 5.3a* (Burlington, MA: COMSOL)
- [36] Miyazato T, Hojo M, Sugano M, Adachi T, Inoue Y, Shikimachi K, Hirano N and Nagaya S 2011 Mode I type delamination fracture toughness of YBCO coated conductor with additional Cu layer *Physica C* **471** 1071–4
- [37] Turon A, Davila C G, Camanho P P and Costa J 2007 An engineering solution for mesh size effects in the simulation of delamination using cohesive zone models *Eng. Fract. Mech.* **74** 1665–82